MATERIALS SCIENCE

Multivalent ions induce lateral structural inhomogeneities in polyelectrolyte brushes

Jing Yu,[1,2,3]* Nicholas E. Jackson,[1,2]* Xin Xu,[4] Blair K. Brettmann,[1,5]† Marina Ruths,[4] Juan J. de Pablo,[1,2] Matthew Tirrell[1,2]

Subtle details about a polyelectrolyte's surrounding environment can dictate its structural features and potential applications. Atomic force microscopy (AFM), surface forces apparatus (SFA) measurements, and coarse-grained molecular dynamics simulations are combined to study the structure of planar polyelectrolyte brushes [poly(styrenesulfonate), PSS] in a variety of solvent conditions. More specifically, AFM images provide a first direct visualization of lateral inhomogeneities on the surface of polyelectrolyte brushes collapsed in solutions containing trivalent counterions. These images are interpreted in the context of a coarse-grained molecular model and are corroborated by accompanying interaction force measurements with the SFA. Our findings indicate that lateral inhomogeneities are absent from PSS brush layers collapsed in a poor solvent without multivalent ions. Together, AFM, SFA, and our molecular model present a detailed picture in which solvophobic and multivalent ion–induced effects work in concert to drive strong phase separation, with electrostatic bridging of polyelectrolyte chains playing an essential role in the collapsed structure formation.

INTRODUCTION

Understanding the response of polyelectrolytes to their environment has challenged materials scientists for decades. Polyelectrolyte brushes are of particular interest because they can regulate transport of ions and molecules (*1*, *2*); control wettability, adhesion, and lubrication of surfaces (*3*, *4*); or convert chemical and biochemical stimuli into optical (*5*), electrical (*6*), and mechanical signals (*7*). In a good solvent without added salt, strong (quenched) polyelectrolyte chains extend away from the grafting surface much more strongly (higher extension) than uncharged chains. When salt is added to the system, the polyelectrolyte brush shrinks substantially (*8*). This change in height is one of the most basic structural changes associated with polyelectrolyte brushes; however, there is also a strong correlation between brush structure and other environmental factors, including solvent quality and pH. A critical understanding of the mechanisms underlying these structural changes upon exposure to external stimuli is vital for the further development of polyelectrolyte brushes and for polyelectrolyte applications at large.

Multivalent ions introduce a level of complexity that is particularly relevant to the interaction of polyelectrolyte brushes with multivalent charged materials such as proteins, nanoparticles, and oppositely charged polyelectrolytes. Previous experimental studies have reported sharp decreases in brush height as a function of the valence and concentration of added multivalent ions (*9*, *10*); these observations have been corroborated by simulations (*11*–*14*) and scaling theory (*15*, *16*). However, the details of the lateral and interior structures of collapsed polyelectrolyte brushes in the presence of multivalent ions remain largely unknown.

The underlying mechanism for polyelectrolyte brush collapse in the presence of multivalent ions remains ambiguous: Is it related to the solvophobic nature of many polyelectrolyte backbones, or is it electrostatically induced among the charged monomers themselves (*17*, *18*)? Counterion condensation occurs more readily for multivalent ions than for monovalent ions, with a predicted fraction of condensed counterions of approximately 90% for trivalent ions (*19*); experimental results indicate an even higher fraction (*20*–*22*). This condensation leaves the polyelectrolyte with a low effective charge, potentially reducing its solubility in water. However, a multivalent ion is also capable of condensing onto multiple polyelectrolyte monomers, which could induce bridges between chains and an alternate type of attraction that may drive polyelectrolyte brush collapse (*15*, *23*, *24*). Understanding the interplay of the solvophobic and multivalent contributions that underlie brush collapse could enable manipulation of these materials.

The study presented here uses a combination of atomic force microscopy (AFM) imaging, surface forces apparatus (SFA) measurements, and molecular dynamics (MD) simulations of a coarse-grained model to directly probe the nature of the lateral and interior structural transitions in planar polyelectrolyte brushes. Polyelectrolyte brushes are imaged using AFM in a variety of solution conditions, including poor solvent and multivalent salt conditions. There is no precedent for these types of observations, particularly the differences between poor solvent and multivalent ion–induced brush structures; thus, our AFM characterization is supplemented with measurements of the interactions between opposing polyelectrolyte brushes with the SFA, where multivalent conditions induce universally repulsive behavior and poor solvent conditions cause a strong adhesive force. Our coarse-grained model allows us to interpret our measurements regarding the nature of polyelectrolyte–multivalent ion interactions at molecular length scales and to separate the effects of backbone solubility from those of electrostatics. These findings provide a comprehensive picture of brush collapse, in which (i) solvophobic collapse and multivalent ion–induced collapse are manifest in distinctly different structural motifs and (ii) the difference between solvophobic and multivalent ion–induced collapse is likely due to the unique nature of multivalent bridging interactions, which produce strongly heterogeneous lateral structures in planar polyelectrolyte brushes.

RESULTS

The polyelectrolyte considered here is sodium poly(styrenesulfonate) (PSS), which, in the context of the synthetic procedure and experimental

[1]Institute for Molecular Engineering, University of Chicago, Chicago, IL 60637, USA. [2]Institute for Molecular Engineering, Argonne National Laboratory, Lemont, IL 60439, USA. [3]School of Materials Science and Engineering, Nanyang Technological University, Singapore 639798, Singapore. [4]Department of Chemistry, University of Massachusetts Lowell, Lowell, MA 01854, USA. [5]School of Materials Science and Engineering, Georgia Institute of Technology, Atlanta, GA 30332, USA.
*These authors contributed equally to this work.
†Corresponding author. Email: blair.brettmann@mse.gatech.edu

conditions of our measurements, is considered a strong polyelectrolyte of unit charge fraction (all monomers are charged) (*9*, *25*). The brushes were formed with high grafting densities (~0.1 chain/nm^2), which exclude the "mushroom" regime and emphasize the importance of neighboring PSS chain interactions. For the studies on multivalent ion–induced collapse in good solvents, simulations were performed at a grafting spacing of 10σ, where σ represents the size of the PSS monomers and ions in the simulation (~0.25 nm). Simulations aimed at assessing the role of good to poor solvent conditions were performed at a grafting spacing of 5σ to accentuate the effects of interchain interactions to better understand the mechanism.

An integral part of this work is the analysis of the relative contributions of solvophobic and electrostatic effects during brush collapse. Discussions concerning solvent quality will refer to experimental solubility, which depends on a combination of the van der Waals solvent quality of the polymer backbone (Flory parameter) and the strength of the charge on the polyelectrolyte. The latter contribution is quantified by the solvent dielectric constant or, more concretely, the Bjerrum length, l_B, the separation at which two charges have an electrostatic interaction of magnitude k_BT (for water at room temperature, l_B is on the order of 0.5 nm). Water was used as a good solvent for PSS, despite it being a poor solvent for the polystyrene backbone, because it has a high dielectric constant (low l_B). Isopropyl alcohol (IPA) was used as a poor solvent for PSS because it is a similarly poor solvent for the polystyrene backbone but has a much lower dielectric constant (high l_B). These solvent variations are fundamental in elucidating the collapse mechanism and provide a strong basis for detailed MD simulations that explore the relative contributions of solvophobic and electrostatic effects.

Structure formation

Most prior experimental studies of multivalent ion–induced brush collapse have been limited to the characterization of the volume fraction as a function of brush height under the assumption of a homogeneously collapsed film. The presence of lateral inhomogeneities was not considered in that body of work. Recent neutron scattering and theoretical investigations have suggested a multivalent ion–collapsed polyelectrolyte brush (*9*) having a polymer volume fraction profile similar to that predicted for a pinned micelle structure of a poor solvent brush (*26*). Such a structure has been confirmed in neutral and weak polyelectrolyte brushes in poor solvents by AFM measurements (*27*–*29*). However, there is no precedent for characterization of the lateral structure of three-dimensional (3D) brushes in multivalent ion solutions.

The PSS brush layer was initially studied in a 6 mM $NaNO_3$ solution (monovalent ion only). Under these conditions, the PSS layer showed large-scale (500 nm wide and 10 nm high) fluctuations in height (Fig. 1A, top) and a relatively uniform corresponding phase image (Fig. 1A, bottom), indicative of uniform viscoelastic response of the layer throughout the entire imaged area. Upon addition of trivalent ions, 0.1 mM $Y(NO_3)_3$, to this system (adjusting the $NaNO_3$ to keep the total ionic strength at 6 mM), heterogeneous features appear on top of the PSS layer, having a typical width of 100 to 200 nm and a typical height of 5 to 10 nm (Fig. 1B, top). The contrast in the corresponding phase image (Fig. 1B, bottom) indicates that a heterogeneous layer has formed, where the higher regions identified in the height images have a different stiffness from the underlying polymer. When the concentration of trivalent ions was increased to 1 mM $Y(NO_3)_3$, strong lateral segregation of the PSS brush surface was observed in Fig. 1C (top), concurrent with strong fluctuations in PSS height (structures with a height of 10 to 20 nm). Again, the corresponding phase image (Fig. 1C, bottom) supports this characterization of a strongly collapsed brush surface with a heterogeneous distribution of PSS viscoelasticity. The results of Fig. 1 are indicative of a collapse process highly sensitive to multivalent ions, in agreement with previous work (*9*, *10*, *23*–*25*, *30*).

Similar changes in the brush layer, but occurring at a lower concentration of trivalent ions, were observed when no monovalent salt ions were present in the system: Structures similar to those in Fig. 1B were formed when going from pure water to 0.01 M $Y(NO_3)_3$ (Fig. 2A and fig. S1).

Previous studies have demonstrated that the extended brush height for a brush collapsed by multivalent ions can be recovered by decreasing the electrostatic screening length (*10*). To examine whether the laterally inhomogeneous structures can transition back to a uniform film, we modulated the local ionic strength via the addition of monovalent salt

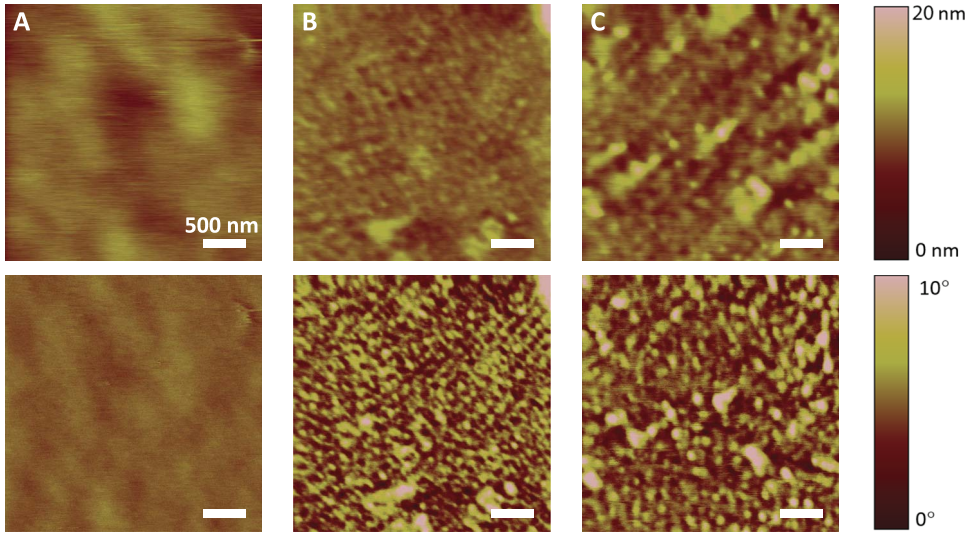

Fig. 1. PSS brush layer structure with and without multivalent ions. AFM tapping mode height (top) and phase images (bottom). (**A**) No distinct features were seen in 6 mM $NaNO_3$ in the absence of multivalent ions, but (**B**) lateral structures formed with the addition of 0.1 mM $Y(NO_3)_3$ (keeping the total ionic strength at 6 mM). (**C**) One millimolar $Y(NO_3)_3$. Scan size, 3 μm × 3 μm (scale bars, 500 nm).

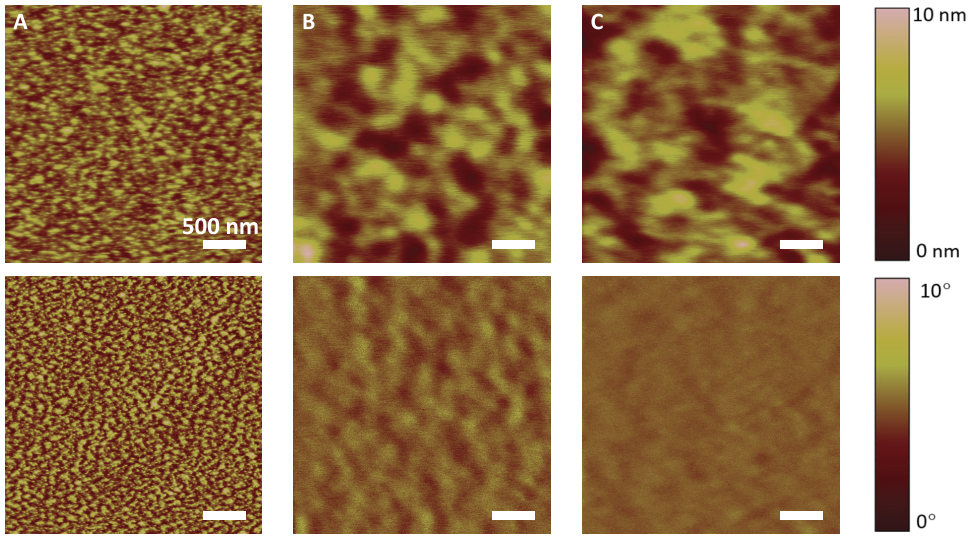

Fig. 2. Collapsed brush layer recovering upon addition of monovalent ions. AFM height (top) and phase (bottom) images showing the effect on PSS brush layers of replacing (**A**) 0.01 mM $Y(NO_3)_3$ in water (no added $NaNO_3$) with increasing concentrations of $NaNO_3$: (**B**) 8 mM $NaNO_3$ and (**C**) 10 mM $NaNO_3$. Scan size, 3 μm × 3 μm (scale bars, 500 nm).

($NaNO_3$) to a sample previously exposed only to 0.01 mM $Y(NO_3)_3$. The addition of varying amounts of monovalent electrolyte promoted the recovery of the homogeneous brush structure (similar to that in Fig. 1A), as shown in Fig. 2 in a sequence of images obtained on the same substrate. In 8 mM $NaNO_3$ (Fig. 2B), the heterogeneous structure only remained over small regions, and in 10 mM $NaNO_3$ (Fig. 2C), it disappeared and only larger-scale fluctuations in height remain (shown here on a different height scale from those in Fig. 1A). The phase images showed the gradual development of a PSS brush of uniform stiffness, which is strongly suggestive of a return to uniformity. Consistent with previous observations of brush heights (*9*, *10*), the structure formation is reversible when the multivalent ions are replaced by monovalent ions.

Given the microscale confirmation of laterally inhomogeneous structure formation in the presence of multivalent ions, it is of interest to examine the molecular-scale behavior of these brushes. For this, a coarse-grained model that includes explicit trivalent counterions was introduced. Figure 3 presents a time-averaged, top-down view of the polyelectrolyte brush density profile as a function of varying salt concentration. All solutions had a background monovalent salt concentration of $5 \times 10^{-3}\ \sigma^{-3}$, with differing amounts of added trivalent salt. For this case, we used a $l_B = 3\sigma$ and a Lennard-Jones (LJ) parameter of 0.4 k_BT, which corresponds to a good solvent. We emphasize again that good solvent conditions were selected for the backbone, despite the dissimilarity with PSS in water experimentally, to separate the solvophobic effect from the trivalent ion effect on collapse.

Under trivalent ion–free conditions (Fig. 3A), the polyelectrolyte brush exhibits a uniform, extended (figs. S2 to S3) morphology, which is maintained at extremely low concentrations of trivalent ions (Fig. 3B), although noticeable localized correlations in the polyelectrolyte brush begin to form, as evidenced by the local increases in polymer density. Once a critical trivalent ion concentration has been surpassed (Fig. 3C), the polyelectrolyte brush collapses (fig. S4 to S5) to form heterogeneous aggregates on the surface. These aggregates are not uniformly shaped and demonstrate the distinct micellar "leg" features observed previously (*31*–*33*). When the trivalent ion concentration approaches a value corresponding to charge neutralization within the brush, the aggregates collapse to more uniform circular globules on the surface. These simulations demonstrate that trivalent ions induce a collapsed structure and that a solvophobic backbone is not a necessary condition for the formation of heterogeneous aggregates.

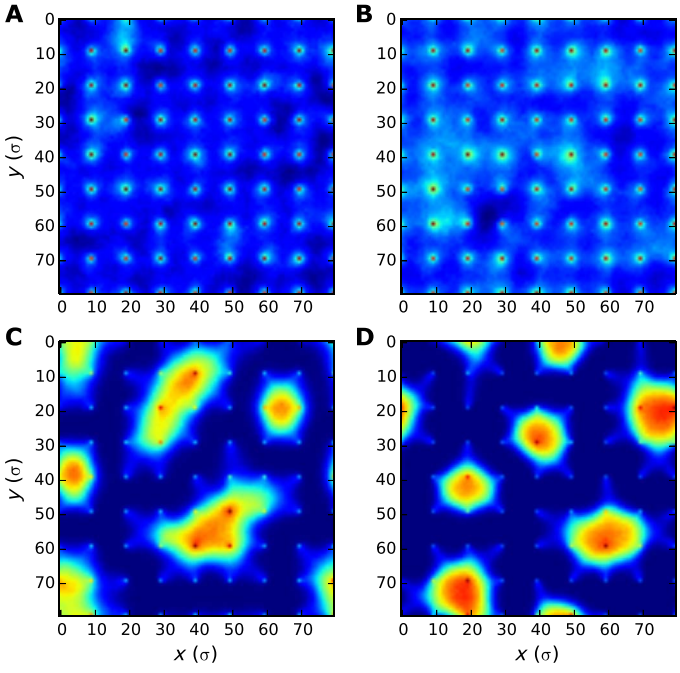

Fig. 3. MD simulation of brush with and without multivalent ions. Top-down view of polymer brush density profile for concentrations of $5 \times 10^{-3}\ \sigma^{-3}$ monovalent salt with (**A**) no trivalent salt, (**B**) $1 \times 10^{-4}\ \sigma^{-3}$ trivalent salt, (**C**) $1 \times 10^{-3}\ \sigma^{-3}$ trivalent salt, and (**D**) $3 \times 10^{-3}\ \sigma^{-3}$ trivalent salt. Color scale corresponds to relative brush densities (red/orange for high density, dark blue for low density), with relative densities scaled to the lowest value of the surface density in each image.

Both the MD simulations and AFM images demonstrate lateral inhomogeneities in the collapsed structure. In the case of Fig. 1B, which represents a regime of trivalent ions where the system is not overly saturated, the system can be qualitatively compared to that of Fig. 3C,

where the charge neutralization point has not yet been reached by the trivalent ion concentration. The AFM results of Fig. 1 suggest an average collapsed feature size of ~100 to 200 nm in the presence of trivalent ions, whereas Fig. 3 (approximating $\sigma \sim 0.25$ nm) suggests a feature size of ~5 to 20 nm. If one considers the differences in molecular weight (MW) (N) between experiment (~10^3) (estimation method described in Materials and Methods) and simulation (10^2) and accounts for the scaling expected for collapsed globules ($N^{1/3}$), then the MW differences account for a factor of 2 to 3 difference in feature size. Given the phenomenological nature of our coarse-grained model, we consider this reasonable agreement.

The simulations were also used to quantify the mobility of counterions within the collapsed globules. The distribution of trivalent ion diffusion coefficients within the collapsed brush demonstrates that nearly 90% of all trivalent counterions are essentially immobilized within the brush and thus contribute little to the osmotic pressure (fig. S6). Simulation results are also in agreement with the qualitative volume fraction profile determined from neutron reflectivity experiments, reproducing the general shape, including the tail at large heights (fig. S7) (*9*). Moreover, our coarse-grained model indicates that multivalent cations are entirely localized within the brush volume, in addition to a small quantity of monovalent cations—this combination of available cations serves to effectively neutralize the total charge of the brush, with multivalent cations being preferentially condensed.

Mechanism of collapse

The results above suggest that polyelectrolyte brushes in multivalent ion solutions collapse into inhomogeneous structures similar to the pinned micelles discussed by Zhulina *et al.* (*26*) and Williams (*33*) for polymers in poor solvents. Poor solvent effects in polyelectrolytes have been studied extensively, both experimentally and theoretically. Critically, past work has shown that the polyelectrolyte brush is expected to collapse into 3D structures, with the particular conformation depending on the grafting density and environmental conditions (*31*, *32*, *34*–*38*). The observed pinned micelle structure formation is also consistent with a recently developed theory for multivalent ion–induced collapse of polyelectrolyte brushes, where the attractions between chains are treated as analogous to attractions in poor solvents but with an effective poor solvent parameter that depends on the valence and bridging strength (*16*).

The similarities between measured and predicted structures in multivalent ion solutions and in poor solvents lead to the question of whether the solvophobic and multivalent collapse mechanisms are more similar than previously thought. Namely, because of very high counterion condensation for multivalent ions [90% condensation predicted via Manning theory (*19*)], it is possible that the solvent quality for the polyelectrolyte with an effective lower charge becomes sufficiently poor to lead to collapse. This would be in contrast to previous assertions that multivalent ion–induced collapse is caused by the bridging of multiple polyelectrolyte chains by a single multivalent ion (*10*, *15*, *24*). The simulation results in Fig. 3 demonstrate that the pinned micelle structure forms under good solvent conditions in the presence of multivalent ions, providing an initial indication that collapse is not solely a poor solvent effect. Below, we contrast the poor solvent and multivalent ion cases more thoroughly and provide a quantitative analysis of multivalent ion bridging to further probe the collapse mechanism.

We first examine the effects of solvent quality on the structural changes in the brush from a microscale perspective and compare these to changes in a brush exposed to multivalent ions. The solvent quality in the PSS brush system was modified by varying the concentrations of isopropanol (IPA) and deionized (DI) water. IPA can be mixed with water in any ratio and is not as good a solvent as water is for PSS, in that the larger l_B causes more significant chain neutralization, leading to a stronger emergence of the solvophobic backbone character (*26*, *31*).

The interaction forces between two PSS brush layers grafted on mica surfaces were measured in a series of IPA/water mixture solutions using the SFA technique. The volume fraction of IPA was sequentially increased from 0 to 100% to gradually decrease the quality of the solvent. In pure DI water and solutions with low concentration of IPA (up to 40% by volume), the interaction was purely repulsive and long-ranged (up to a distance of 700 nm), showing no hysteresis during the whole compression separation cycle (Fig. 4A). The PSS brushes are in the osmotic regime in pure DI water. The long-range repulsion measured is due to the osmotic pressure of the monovalent counterions (Na^+) that balances the elasticity of the PSS chains. Scaling theory shows that the range of the repulsion is proportional to the MW of the PSS chains but

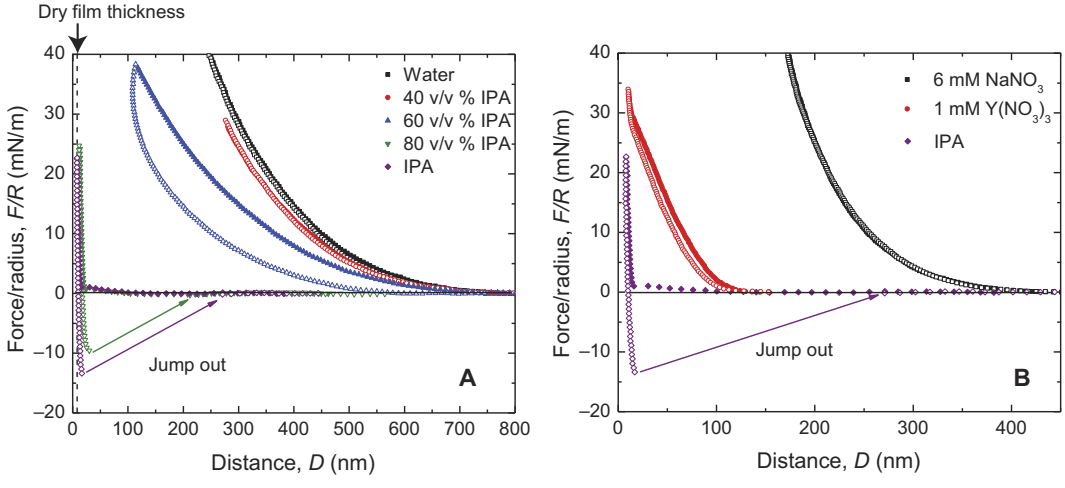

Fig. 4. SFA force distance curves during compression and separation of two identical PSS brush layers. (**A**) In mixed IPA/water solutions with IPA volume fractions of 0, 40, 60, 80, and 100%, respectively. (**B**) In 6 mM $NaNO_3$, 1 mM $Y(NO_3)_3$, and pure IPA solutions. Solid data points represent forces upon compression, and open data points were measured upon separation of the brush layers.

independent of the grafting density (*8*). Increasing the volume fraction of IPA to 60% significantly changed the force distance curve, which then showed a much shorter range of repulsion during the compression and strong hysteresis during the separation. Further increasing the IPA content to 80% completely removed the long-range repulsion. The force-distance curve shows a hard-wall cutoff: At distances above 10 nm, there is no strong repulsion, and below 10 nm, the repulsion rapidly increases. In addition, a strong adhesion force of −10 mN/m is measured upon separating the surfaces, evident by the sudden jump apart of the two surfaces to about 200 nm. This adhesion is expected for separating two polymer films in a poor solvent (*39*). The force measured in pure IPA is almost identical to that measured in 80% IPA, with a slightly smaller hard-wall distance (9 nm) and a stronger adhesion force (−12 mN/m). This hard-wall distance is the same as the thickness of two dry PSS films (in the absence of solvent), suggesting that the PSS brushes collapse into condensed films in IPA. The measured adhesion force between the collapsed layers is in agreement with that expected to arise from the van der Waals forces between pure PSS interacting across pure IPA (−12 mN/m based on bulk refractive indexes and dielectric constants of the materials) (*40*), consistent with the formation of smooth, compact PSS layers as suggested by the force curves and seen in the AFM images.

The SFA force curves in Fig. 4A reveal that the collapsed PSS brushes in a poor solvent have a very different structure from those in solutions containing multivalent counterions (Fig. 4B). The range of repulsion decreases from about 400 to 120 nm upon replacing a 6 mM $NaNO_3$ solution with a 1 mM $Y(NO_3)_3$ solution, indicating that the PSS brushes undergo a rapid shrinkage in the presence of trivalent Y^{3+} ions. The repulsion gradually increases upon further compression of the two surfaces, and the force is purely repulsive during the whole compression-separation cycle, in contrast to the contact in pure IPA, which displays a step function–like force distance curve and a strong adhesion (−12 mN/m) on separation. This type of interaction was expected for the fully extended brush, but in the case of the collapsed layers, the observation of monotonic repulsion on both compression and separation is indicative of the presence of surface roughness: Any attraction between nearly neutral collapsed chains is masked by repulsive forces from compression of asperities of different heights on the rough surface structure. The observation of such interaction forces is therefore consistent with the AFM images of multivalent ion–collapsed layers.

The differences in structure between brushes collapsed via poor solvent interactions and multivalent ion interactions can also be confirmed using AFM. The height and phase images obtained in solutions with a volume fraction of 80% IPA are shown in Fig. 5. Very similar images were obtained in 100% IPA (fig. S8). This brush layer is clearly a homogeneous film and does not display the many lateral inhomogeneities that are evident in Fig. 1 (B and C). Also note that the gradual undulations seen in the extended (noncollapsed) brush in Fig. 1A were not observed; instead, the film appears uniform and similar to other homogeneous collapsed brush layers (*41*, *42*), including the featureless film formed by dry, as-synthesized PSS brushes (*25*). The AFM results in the poor solvent system in this study are thus differentiable from those pertaining to the multivalent system.

Although experimentally we are limited in our ability to separate the effects of van der Waals solvent quality (Flory parameter) from charge-induced solubility (a low l_B will cause the polyelectrolyte to behave as if it is more soluble and a high l_B will cause it to behave as if it is less soluble), we can separate these effects in our model. IPA has only a minor effect on the van der Waals solvent quality of the PSS backbone when compared to pure water but increases the solvent l_B by a factor of ~4. Figure 6 shows brushes simulated under salt-free conditions with a l_B roughly corresponding to that of IPA (12σ) with a solvophilic (Fig. 6A) and solvophobic (Fig. 6B) backbone. If the mechanism of polyelectrolyte collapse was independent of the valence of the ions, this renormalized l_B should lead to a similarly collapsed and heterogeneously phase-separated structure, as seen in multivalent ion

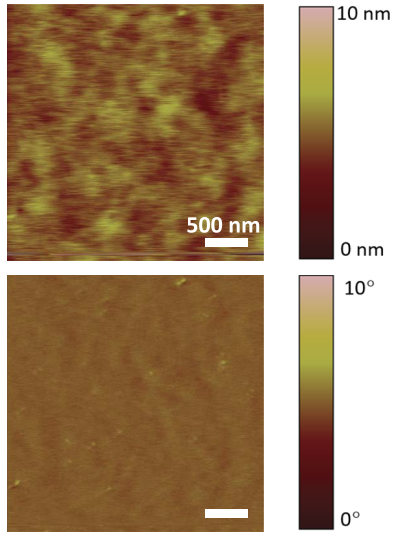

Fig. 5. Collapsed PSS brush layer in poor solvent. Height (**top**) and phase (**bottom**) image of PSS brushes in 80% IPA solution. Scan size, 3 μm × 3 μm (scale bars, 500 nm).

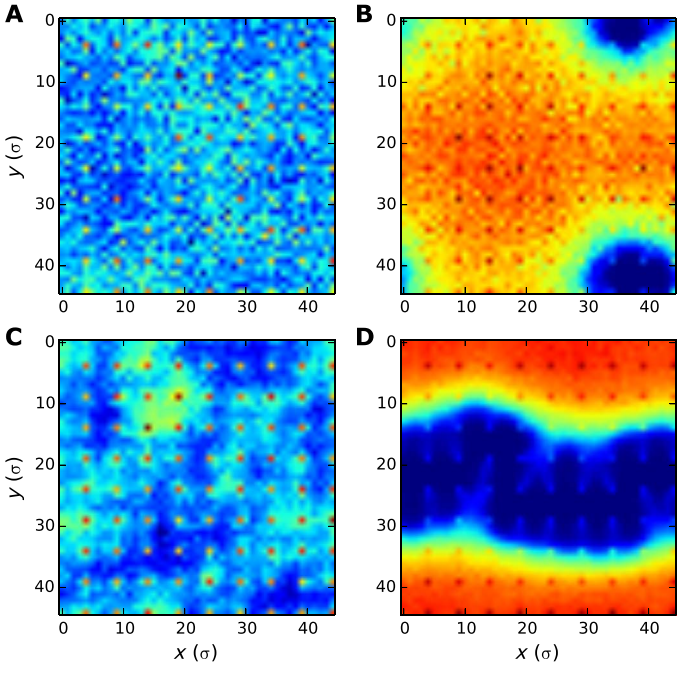

Fig. 6. MD simulation of brushes with solvophilic or solvophobic backbone. Top-down view of periodic polymer brush density profile at a grafting separation of 5σ for (**A** and **B**) salt-free, l_B = 12σ conditions with (A) good solvent (0.4 k_BT) and (B) poor solvent (1.4 k_BT) LJ interactions. (**C** and **D**) Trivalent salt (2×10^{-3} σ^{-3}), l_B = 3σ, with (C) good solvent (0.4 k_BT) and (D) poor solvent (1.4 k_BT) LJ interactions. Color scale corresponds to relative brush densities (red/orange for high density, dark blue for low density), with relative densities scaled to the lowest value of the surface density in each image.

solutions with a lower l_B (Fig. 3C). The brushes are indeed collapsed (figs. S9 to S10); however, although some very small (<10σ) inhomogeneities in the brush surface are observed in Fig. 6B, there is no evidence for an unambiguous phase separation, supporting the poor solvent AFM condition experiments in Fig. 5 where a compressed, uniform film was observed.

Figure 6C shows the brush density profile under solvophilic backbone conditions (LJ, 0.4 k_BT), with a l_B corresponding to water (3σ) and a concentration of 2×10^{-3} σ^{-3} trivalent ions. It is apparent that the trivalent ions alone are capable of inducing collapse (fig. S11) and minor brush inhomogeneities but are not enough to cause the distinct lateral phase separation observed experimentally. However, as is well known, the backbone of PSS is highly solvophobic in water. To account for this, in Fig. 6D, the brush density is simulated using solvophobic backbone conditions (1.4 k_BT) and trivalent ions. In this situation, remarkable lateral phase separation is observed (Fig. 6D and fig. S12), similar to that seen in the AFM results, but with larger-scale separation. These results support (i) the fact that increasing l_B (such as with IPA) in the absence of trivalent ions leads to relatively uniformly collapsed films (no lateral phase separation is observed) and (ii) the finding that the lateral phase separation observed in the AFM can be properly accounted for through a combination of the effects of trivalent ions and the solvophobic nature of the PSS backbone. The molecular model suggests that although both trivalent and solvophobic effects can provide independent brush collapse mechanisms, the lateral phase separation observed experimentally is likely due to the combined solvophobic nature of the PSS backbone and trivalent effects.

Although all simulations in Figs. 3, 6, and 7 assume a monodisperse distribution of polymer chain MWs, simulations in the Supplementary Materials (figs. S13 to S20) explore the impact of polydispersity on the brush morphologies. Polydispersity has no discernible effect at the low grafting densities (fig. S13 to S16), but at higher grafting densities (figs. S17 to S20), the inherent surface roughness associated with a polydisperse distribution of chain lengths enhances the presence of the observed spatial heterogeneities. However, it is important to note that polydispersity by itself is incapable of leading to the drastic lateral phase separation observed only in the presence of trivalent ions, as indicated by the low grafting density simulations.

Given the importance of multivalent counterion interactions established above, simulations were also used to quantify and better understand the molecular-scale, electrostatic bridging of different polyelectrolyte chains by a single multivalent ion. Bridging was quantified by means of a topological distance parameter, α, described in Materials and Methods. The α parameter serves as a simple metric for gauging whether the negatively charged polyelectrolyte monomers condensed around a trivalent ion are topologically near each other. Large values of α (≥5) indicate topologically distant polyelectrolyte monomers condensed around the same trivalent ion (interchain bridging), whereas low values of α correspond to nearest neighbor condensation; intermediate values of α correspond to monomers on the same chain but topologically distant from each other, as illustrated in Fig. 7A. In Fig. 7B, all values of α larger than 5 are collected into the bin at 5α.

Figure 7B shows the distribution of α under solvophilic backbone conditions at a trivalent ion concentration of 10^{-4} σ^{-3}; the use of solvophilic backbone conditions is chosen to help analyze the specific contributions of trivalent ions to collapse. This low trivalent ion concentration allows for the examination of bridging before total collapse. At this concentration, 35% of all trivalent ions are observed to be "bridging" different polyelectrolyte chains, whereas the rest are condensed by monomers from the same chain, albeit at a distribution of topological distances. This result can be contrasted with that of Fig. 7C, conducted at a trivalent ion concentration of 10^{-3} σ^{-3}, which is sufficient to observe near-complete polyelectrolyte brush collapse. In this case, nearly 90% of all trivalent ions exhibit an interchain bridging character, indicating that the collapse of the polyelectrolyte brush is partially due to interchain attractions mediated by trivalent ions. The remaining 10% of the trivalent ions exist in some form of intrachain condensation, similar to Fig. 7A.

DISCUSSION

Microscale AFM experiments and molecular-level simulations show that the brush collapses into 3D, laterally inhomogeneous structures, in agreement with predictions of simple theories (*16*). A qualitatively similar distribution of collapsed feature shapes was observed experimentally (Fig. 1) and computationally (Fig. 3), with the clear existence of nonuniform surface micelle-like structures. These structures strongly resemble those predicted for polymer and polyelectrolyte brushes in poor solvents (*26*, *33*, *34*), providing evidence that there may be analogies between the short-range attractions in poor solvents and those induced by multivalent ion bridging or that the collapse itself may be caused by solvophobic interactions.

However, detailed experimental SFA and AFM studies comparing collapse in poor solvents to collapse in multivalent ion solutions show that there are significant differences in the structures formed in each case, and simulations confirm that the strongly phase-separated 3D structures appear when both poor solvent conditions for the backbone and multivalent ions are present. The SFA measurements demonstrate that the interaction forces between fully extended polyelectrolyte brush layers and multivalent ion–collapsed ones are always repulsive (upon both compression and separation of the layers), whereas the interaction forces are adhesive for surfaces in poor solvents, indicative of uniformly collapsed films. The nature of the collapse was probed further through quantification of bridging interactions by multivalent ions. At both low and high multivalent ion concentrations, bridging is present, but for high concentrations corresponding to the collapsed state, nearly 90% of multivalent ions are engaged in interchain bridging. The attraction of separate polyelectrolyte chains because of multivalent ion bridging is indeed a key driver for collapse and formation of lateral inhomogeneities and should be an important target for future studies. Both experimental studies that can quantify the extent of bridging and verify the results from the molecular-level calculations presented here would help understand the precise nature of the bridging interactions, including ion-specific effects and local dielectric environment.

Through a combination of direct imaging, microscale force measurements, and molecular simulations, this work concretely demonstrates that the exposure of polyelectrolyte brushes to multivalent ions leads to the formation of lateral inhomogeneities. This work provides a first step toward experimental verification of this phenomenon, and it will be important to supplement it with additional work that relies on alternative characterization techniques, including scattering. We conclude that poor solvent effects and multivalent ionic bridging combine to contribute to the strong phase separation observed experimentally. Critically, we have demonstrated that bridging plays a key role in collapse, showing that multivalent ions closely attract to monomers on different brush chains.

Our analysis of the behavior of polyelectrolyte brushes in the presence of multivalent ions might affect materials science on several fronts.

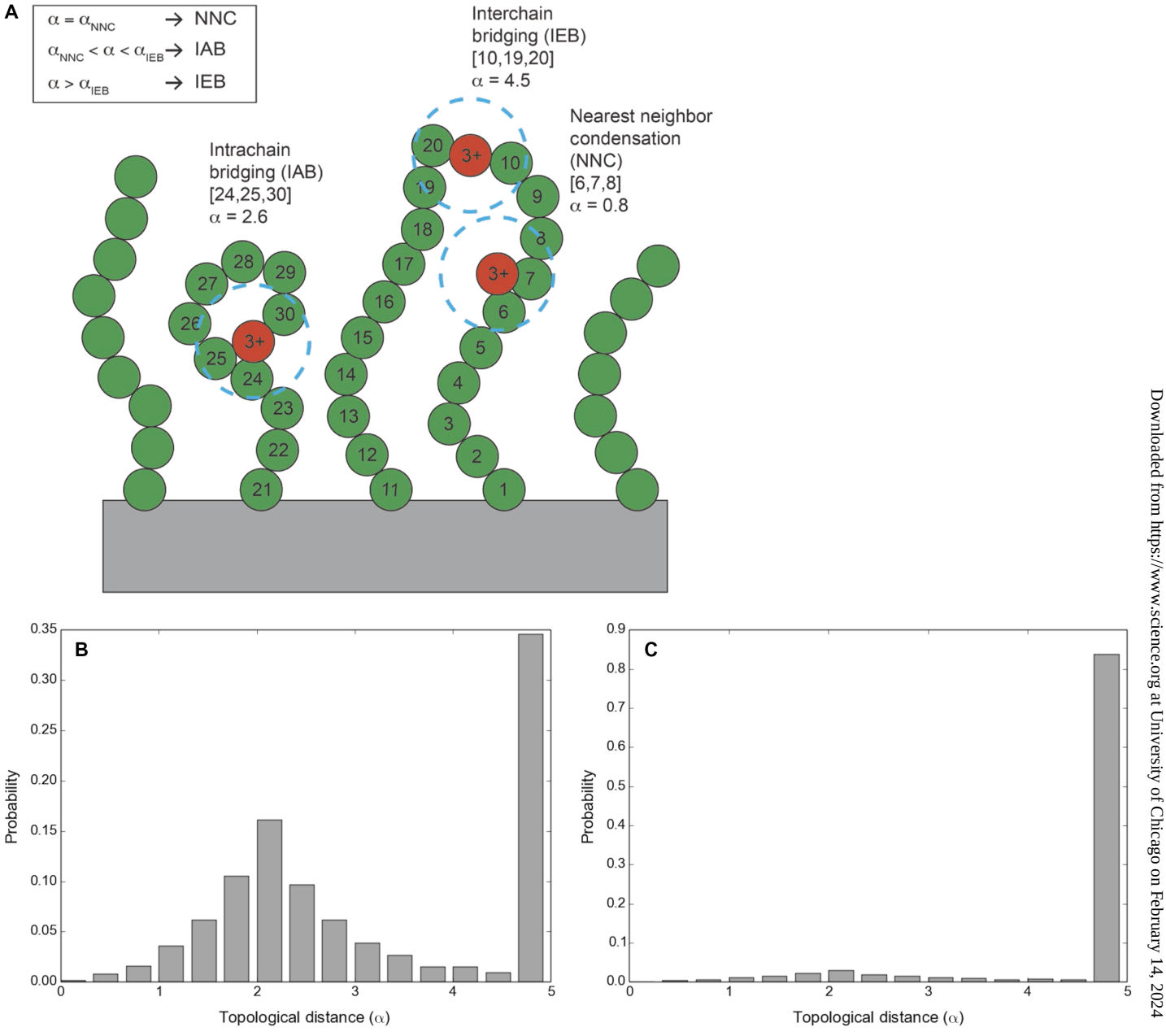

Fig. 7. Interaction of multivalent ions with polyelectrolyte chains. (**A**) Molecular-level model. Distribution of topological distances (α) for bridging in polyelectrolyte brushes at trivalent ion concentrations of (**B**) 10^{-4} σ^{-3} and (**C**) 10^{-3} σ^{-3}, corresponding to the conditions of Fig. 3 (B and C, respectively). Values of $\alpha \geq 5$ denote trivalent ions involved in interchain bridging.

The potential for new stimuli-responsive microstructured surfaces is particularly exciting. Polyelectrolyte brushes provide lubrication in many biological and technical systems (*43*, *44*), and microscale structure formation will strongly affect friction forces between coated surfaces. In addition, functional brushes, such as DNA brushes being used as artificial cell compartments for production of biomolecules (*2*, *7*), will experience changes in functionality as surface structures are formed. As such, the fundamental analysis presented here provides a foundation for the design of new surfaces for a variety of technical, biological, and biomedical applications.

MATERIALS AND METHODS

Materials

Sodium 4-vinylbenzenesulfonate (SSNa) (technical, ≥90%), 3-aminopropyltriethoxysilane (APTES, 99%), α-bromoisobutyryl bromide (BIBB, 98%), triethylamine (≥99%), 2,2-bipyridyl (bpy, ≥99%), Cu(I)Br (99.999%), tetrahydrofuran (THF) (anhydrous, 99.8%), methanol (≥99.9%), IPA (99.7%), sodium nitrate (99%), and yttrium nitrate hexahydrate (99.8%) were purchased from Aldrich and used without further purification. DI water was obtained from a Millipore Milli-Q system with a resistivity of 18.2 megohm·cm.

Synthesis of PSSNa brushes

The synthesis of PSSNa polymer brush layers was performed via surface-initiated atom transfer radical polymerization (SI-ATRP) using a reported procedure (*25*). On silicon substrates (used for AFM samples), a layer of APTES was first deposited onto a Piranha-cleaned silicon wafer via vapor deposition. Caution: Piranha solution is highly corrosive and should be handled with care. Mica surfaces (for SFA) were treated with argon/water vapor plasma for 30 min to create hydroxyl groups before the APTES deposition. After annealing, an ATRP initiator (BIBB) was grafted to the APTES monolayer from THF solution. SI-ATRP grafting of PSSNa was carried out in a 1:1 mixture of methanol and water (50 ml) containing SSNa (5 g, 24.2 mmol), Cu(I)Br (35 mg, 0.24 mmol), and bpy (75 mg, 0.48 mmol). The SI-ATRP method can give densely tethered PSS brushes with well-controlled brush height. The total dry thickness of two PSS brushes on mica (in contact in the SFA) was around 10 nm. The grafting density of the PSS brush was estimated to be about 0.1 chain/nm^2 on silicon and 0.025 chain/nm^2 on mica (*25*).

MW calculation

The MW and grafting density of the PSS brushes on silicon wafers can be estimated by comparing the brush height in water and dry thickness of our PSS film to our previous SFA results on sparsely tethered PSS brushes generated via physisorption of diblock poly t-butyl styrene (PtBS)20-PSSNa420 polymer, which had 420 segments of PSSNa (*23*). In the osmotic regime, the thickness of the brush is given by $H \sim Nf^{0.5}$, where N is the degree of polymerization of the polyelectrolyte chain and f is the fraction of charged monomers (for PSS, $f = 1$). In the osmotic regime, H is independent of the grafting density (*8*). The height of the sparsely tethered PSS brush (H_1) was ~100 nm. The heights of the PSS brushes used in the current study (H_2) were between 200 and 300 nm (depending on different batches of samples). The degree of polymerization of the PSS chain used in this study can be estimated by $N_2 \sim \frac{H_2}{H_1} N_1 \sim 800$ to 1200, that is, of the order of 1000. The polydispersity is expected to be lower than 1.25 as is typically observed for SI-ATRP (*45*, *46*).

Similarly, we obtained the PSS brush grafting density by comparing the dry film thickness data to the physisorbed PtBS-PSS brushes. Our previous sparely tethered PSS brush had a dry film thickness of 1 nm, which was equivalent to a mass density of $m_1 = 1$ mg/m^2 (assuming the density of dry PSS is ~1 g/cm^3). The grafting density is 1 chain per 100 nm^2, or $d_1 = 0.01$ chain/nm^2. A typical dry film thickness of the PSS brushes on silicon surface used in this study was around 20 nm, and the mass density was $m_2 = 20$ mg/m^2. The height of the sparsely tethered PSS brush (H_1) in solution was about 100 nm (*23*), and the height of the densely tethered PSS brush (H_2) was about 200 nm [measured by neutron reflectivity, see the study of Yu *et al.* (*9*)]. The mass density of the PSS brush can be calculated by $m_1 = A\, d_1 H_1$ and $m_2 = A\, d_2 H_2$, in which A is a constant. Comparing m_1 and m_2, we can get $d_2 = 0.1$ chain/nm^2 as an estimate of the grafting density of our densely tethered PSS brushes. This is consistent with the grafting density (0.1 to 0.3 chain/nm^2) reported by others using SI-ATRP (*47*). The grafting density of the PSS brushes on mica surface was about 0.025 chain/nm^2, calculated using the same method.

Surface forces apparatus

The normal forces between two PSS brushes grafted on mica were measured using an SFA (SFA2000, SurForce LLC) (*48*). Freshly cleaved mica sheets (thickness, ~2 to 5 μm) were glued to cylindrical glass disks ($R = 2$ cm) using ultraviolet-curable optical glue. The synthesis of PSS brushes on mica is described above. Interaction forces between two PSS brushes in solution were measured as a function of the distance between the apposing mica surfaces in a cross-cylinder geometry, which, at small separation distances, is equivalent to a spherical surface interacting with a flat surface. The approach and separation speed of our SFA measurements was about 4 nm/s. Upon changing solutions, the old solution in the SFA chamber was completely drained, and the SFA chamber was then flushed with the new solution three times to fully remove the old solution. The surface force results were based on two independent experiments. Two to three repeating force measurements were performed for each condition in each of the experiment.

Atomic force microscopy

The PSS brush layers on silicon were stored in a desiccator when not used for AFM experiments. Tapping mode height (topology) and phase images of the brush layers in water and electrolyte solutions were acquired with a Nanoscope IV Multimode AFM (Bruker). The scan rate was 0.8 to 1.5 Hz. The AFM cantilevers (CSC17/Cr-Au, MikroMasch) had a resonance frequency of about 12 kHz in air and 4 to 5 kHz in liquid. The tip radius was typically 20 to 30 nm. The effects of tip convolution on the measured width of the imaged features were estimated as $w^2 = 8Rh$, where w is the broadening, R is the tip radius, and h is the height of the feature on the surface. For typical values of R and h ($h = 10$ nm), w was in the 45- to 50-nm range, which was the tip contribution to the measured widths of the features. All AFM experiments were performed at room temperature (ca. 22°C).

MD simulations

Simulations applied a commonly used model for polyelectrolytes (*49*). Sixty-four polyelectrolyte chains of 100 spherical charged LJ beads of diameter σ were grafted to a surface of cubic lattice points. To set the length scale of the simulations, we assumed σ = 0.23 nm, which was obtained by matching the simulated l_B (3σ) to the experimental l_B for water at 300 K (0.7 nm). Using this value for σ, the estimated grafting density for 5σ and 10σ spacing is ~0.2 and ~0.8 chains/nm^2, respectively. Provided that our chain MW is a factor of ~10 smaller than that in the experiments, this increased grafting density relative to the experiments is a reasonable approximation for the experimental system. Each bead in the polymer chain was bonded to its nearest neighbor using the finite extensible nonlinear elastic potential having an average bond length of 1.1σ. A polyelectrolyte persistence length of 1σ was enforced using a three-body cosine-δ bending potential between neighboring monomers. This system of 6400 polyelectrolyte beads was in equilibrium with 6400 monovalent counterion beads (representative of salt particles in solution), embedded in a dielectric environment corresponding to the l_B (we assumed $l_B = 3\sigma$ for standard water and $l_B = 12\sigma$ for IPA). Extra salt particles were added to the simulation cell corresponding to the monovalent/trivalent salt concentrations of the solution. Electrostatic interactions were treated using a P3M Ewald sum in the slab geometry, with solvent fluctuations incorporated via a Langevin thermostat. Dynamics were evolved using the velocity-Verlet algorithm. Two million time steps of 0.005τ were run for polyelectrolyte brush equilibration, with 5 million steps for the production run. Periodic boundary conditions were applied in the dimensions parallel to the substrate, and impenetrable walls were placed at $z = 0$ and $z = 200\sigma$.

Bridging analysis

A bridging parameter α that measured the topological distance between neighboring polymer monomers condensed around a trivalent ion was

defined. The system consisted of M-grafted chains, with each chain containing N monomers assigned a unique integer i that increased linearly along the length of the chain. After one chain had been assigned numbers (1, 2…, N), a neighboring polymer chain was selected, and the integer i was assigned along that chain, beginning with the last value from the previous chain (N + 1, N + 2…, 2*N). This process was continued until all monomers in the brush were uniquely enumerated.

To analyze the brush system, we selected a particular trivalent ion in the MD trajectory snapshot. We searched for all polymer monomers within a cutoff distance (r_c) of that trivalent ion's position and formed a neighbor list ({NL}) (referred to as topological indices) of all of the polymer monomers within r_c. Here, we used a stringent r_c of $2^{1/2}$. Provided this neighbor list, we needed a means of discriminating whether this list corresponds to nearest neighbor condensation, intrachain bridging, or interchain bridging. To this end, we took the SD of the neighbor list (unique numbers corresponding to polymer monomers) around a particular trivalent ion

$$\alpha = \sqrt{\frac{1}{\mathrm{len}(\{\mathrm{NL}\})}\sum_{i}^{\{\mathrm{NL}\}}(i-\bar{i})^2}$$

where len({NL}) is the length of the neighbor list, i is the topological index of the polymeric monomer, and $\bar{i}$ is the mean topological index of the neighbor list. The SD of this list gives a rough sense of the topological "distance" between polymer monomers "condensed" around a trivalent ion. By comparing the computed value of the list SD for each examined trivalent ion to precomputed values corresponding to particular MW polymer brushes, we can select whether that trivalent ion is involved in bridging based on the topological SD of that list.

SUPPLEMENTARY MATERIALS

Supplementary material for this article is available at http://advances.sciencemag.org/cgi/content/full/3/12/eaao1497/DC1

AFM imaging in solution

fig. S1. AFM images of PSS brush layers in the absence and presence of multivalent ions.

fig. S2. Charge distribution and polymer density plots corresponding to the data presented in Fig. 3A.

fig. S3. Charge distribution and polymer density plots corresponding to the data presented in Fig. 3B.

fig. S4. Charge distribution and polymer density plots corresponding to the data presented in Fig. 3C.

fig. S5. Charge distribution and polymer density plots corresponding to the data presented in Fig. 3D.

fig. S6. Distribution of diffusion rates of trivalent ions in the collapsed brush systems.

fig. S7. Distributions of polyelectrolytes and ions in a brush layer.

fig. S8. Collapsed PSS brush layer in poor solvent.

fig. S9. Charge distribution and polymer density plots corresponding to the data presented in Fig. 6A.

fig. S10. Charge distribution and polymer density plots corresponding to the data presented in Fig. 6B.

fig. S11. Charge distribution and polymer density plots corresponding to the data presented in Fig. 6C.

fig. S12. Charge distribution and polymer density plots corresponding to the data presented in Fig. 6D.

fig. S13. Polymer density plots for the polydisperse simulation using conditions corresponding to Fig. 3A.

fig. S14. Polymer density plots for the polydisperse simulation using conditions corresponding to Fig. 3B.

fig. S15. Polymer density plots for the polydisperse simulation using conditions corresponding to Fig. 3C.

fig. S16. Polymer density plots for the polydisperse simulation using conditions corresponding to Fig. 3D.

fig. S17. Polymer density plots for the polydisperse simulation using conditions corresponding to Fig. 6A.

fig. S18. Polymer density plots for the polydisperse simulation using conditions corresponding to Fig. 6B.

fig. S19. Polymer density plots for the polydisperse simulation using conditions corresponding to Fig. 6C.

fig. S20. Polymer density plots for the polydisperse simulation using conditions corresponding to Fig. 6D.

Representative large-scale atomic/molecular massively parallel simulator input (used to generate data in Fig. 6C).

REFERENCES AND NOTES

1. N. Welsch, Y. Lu, J. Dzubiella, M. Ballauff, Adsorption of proteins to functional polymeric nanoparticles. *Polymer* **54**, 2835–2849 (2013).
2. E. Karzbrun, A. M. Tayar, V. Noireaux, R. H. Bar-Ziv, Programmable on-chip DNA compartments as artificial cells. *Science* **345**, 829–832 (2014).
3. M. Kobayashi, Y. Terayama, H. Yamaguchi, M. Terada, D. Murakami, K. Ishihara, A. Takahara, Wettability and antifouling behavior on the surfaces of superhydrophilic polymer brushes. *Langmuir* **28**, 7212–7222 (2012).
4. U. Raviv, S. Giasson, N. Kampf, J.-F. Gohy, R. Jérôme, J. Klein, Lubrication by charged polymers. *Nature* **425**, 163–165 (2003).
5. R. Fan, O. Vermesh, A. Srivastava, B. K. H. Yen, L. Qin, H. Ahmad, G. A. Kwong, C.-C. Liu, J. Gould, L. Hood, J. R. Heath, Integrated barcode chips for rapid, multiplexed analysis of proteins in microliter quantities of blood. *Nat. Biotechnol.* **26**, 1373–1378 (2008).
6. T. G. Drummond, M. G. Hill, J. K. Barton, Electrochemical DNA sensors. *Nat. Biotechnol.* **21**, 1192–1199 (2003).
7. D. Bracha, E. Karzbrun, G. Shemer, P. A. Pincus, R. H. Bar-Ziv, Entropy-driven collective interactions in DNA brushes on a biochip. *Proc. Natl. Acad. Sci. U.S.A.* **110**, 4534–4538 (2013).
8. P. Pincus, Colloid stabilization with grafted polyelectrolytes. *Macromolecules* **24**, 2912–2919 (1991).
9. J. Yu, J. Mao, G. Yuan, S. Satija, Z. Jiang, W. Chen, M. Tirrell, Structure of polyelectrolyte brushes in the presence of multivalent counterions. *Macromolecules* **49**, 5609–5617 (2016).
10. R. Farina, N. Laugel, J. Yu, M. Tirrell, Reversible adhesion with polyelectrolyte brushes tailored via the uptake and release of trivalent lanthanum ions. *J. Phys. Chem. C* **119**, 14805–14814 (2015).
11. V. S. Guptha, P.-Y. Hsiao, Polyelectrolyte brushes in monovalent and multivalent salt solutions. *Polymer* **55**, 2900–2912 (2014).
12. N. E. Jackson, B. K. Brettmann, V. Vishwanath, M. Tirrell, J. J. de Pablo, Comparing solvophobic and multivalent induced collapse in polyelectrolyte brushes. *ACS Macro Lett.* **6**, 155–160 (2017).
13. Q.-H. Hao, Q. Chen, Z. Zheng, L.-Y. Liu, T.-J. Liu, X.-H. Niu, Q.-G. Song, H.-G. Tan, Molecular dynamics simulations of cylindrical polyelectrolyte brushes in monovalent and multivalent salt solutions. *J. Theor. Comput. Chem.* **15**, 1650026 (2016).
14. L. Liu, P. A. Pincus, C. Hyeon, Heterogeneous morphology and dynamics of polyelectrolyte brush condensates in trivalent counterion solution. *Macromolecules* **50**, 1579–1588 (2017).
15. B. K. Brettmann, N. Laugel, N. Hoffmann, P. Pincus, M. Tirrell, Bridging contributions to polyelectrolyte brush collapse in multivalent salt solutions. *J. Polym. Sci. A Polym. Chem.* **54**, 284–291 (2016).
16. B. Brettmann, P. Pincus, M. Tirrell, Lateral structure formation in polyelectrolyte brushes induced by multivalent ions. *Macromolecules* **50**, 1225–1235 (2017).
17. R. Zhang, N. F. A. van der Vegt, Study of hydrophobic clustering in partially sulfonated polystyrene solutions with a systematic coarse-grained model. *Macromolecules* **49**, 7571–7580 (2016).
18. N. Lee, D. Thirumalai, Dynamics of collapse of flexible polyelectrolytes in poor solvents. *Macromolecules* **34**, 3446–3457 (2001).
19. G. S. Manning, Limiting laws and counterion condensation in polyelectrolyte solutions I. Colligative properties. *J. Chem. Phys.* **51**, 924–933 (1969).
20. I. Sabbagh, M. Delsanti, P. Lesieur, Ionic distribution and polymer conformation, near phase separation, in sodium polyacrylate/divalent cations mixtures: Small angle X-ray and neutron scattering. *Eur. Phys. J. B.* **12**, 253–260 (1999).
21. R. Schweins, G. Goerigk, K. Huber, Shrinking of anionic polyacrylate coils induced by Ca^{2+}, Sr^{2+} and Ba^{2+}: A combined light scattering and ASAXS study. *Eur. Phys. J. E. Soft Matter* **21**, 99–110 (2006).
22. T. E. Angelini, L. K. Sanders, H. Liang, W. Wriggers, J. X. Tang, G. C. L. Wong, Structure and dynamics of condensed multivalent ions within polyelectrolyte bundles: A combined x-ray diffraction and solid-state NMR study. *J. Phys. Condens. Matter* **17**, S1123–S1135 (2005).
23. R. Farina, N. Laugel, P. Pincus, M. Tirrell, Brushes of strong polyelectrolytes in mixed mono- and tri-valent ionic media at fixed total ionic strengths. *Soft Matter* **9**, 10458–10472 (2013).
24. Y. Mei, K. Lauterbach, M. Hoffmann, O. V. Borisov, M. Ballauff, A. Jusufi, Collapse of spherical polyelectrolyte brushes in the presence of multivalent counterions. *Phys. Rev. Lett.* **97**, 158301 (2006).

25. J. Yu, J. Mao, G. Yuan, S. Satija, W. Chen, M. Tirrell, The effect of multivalent counterions to the structure of highly dense polystyrene sulfonate brushes. *Polymer* **98**, 448–453 (2016).
26. E. Zhulina, C. Singh, A. C. Balazs, Behavior of tethered polyelectrolytes in poor solvents. *J. Chem. Phys.* **108**, 1175–1183 (1998).
27. N. Backmann, N. Kappeler, T. Braun, F. Huber, H.-P. Lang, C. Gerber, R. Y. H. Lim, Sensing surface PEGylation with microcantilevers. *Beilstein J. Nanotechnol.* **1**, 3–13 (2010).
28. K. N. Witte, J. Hur, W. Sun, S. Kim, Y.-Y. Won, Evidence of lateral nanoscale heterogeneities in weak polyelectrolyte brushes. *Macromolecules* **41**, 8960–8963 (2008).
29. J. Hur, K. N. Witte, W. Sun, Y.-Y. Won, On the origins of the salt-concentration-dependent instability and lateral nanoscale heterogeneities of weak polyelectrolyte brushes: Gradient brush experiment and Flory-type theoretical analysis. *Langmuir* **26**, 2021–2034 (2010).
30. Y. Mei, M. Hoffmann, M. Ballauff, A. Jusufi, Spherical polyelectrolyte brushes in the presence of multivalent counterions: The effect of fluctuations and correlations as determined by molecular dynamics simulations. *Phys. Rev. E. Stat. Nonlin. Soft Matter Phys.* **77**, 031805 (2008).
31. J.-M. Y. Carrillo, A. V. Dobrynin, Morphologies of planar polyelectrolyte brushes in a poor solvent: Molecular dynamics simulations and scaling analysis. *Langmuir* **25**, 13158–13168 (2009).
32. D. J. Sandberg, J.-M. Y. Carrillo, A. V. Dobrynin, Molecular dynamics simulations of polyelectrolyte brushes: From single chains to bundles of chains. *Langmuir* **23**, 12716–12728 (2007).
33. D. R. M. Williams, Grafted polymers in bad solvents: Octopus surface micelles. *J. Phys. II* **3**, 1313–1318 (1993).
34. R. M. Choueiri, E. Galati, H. Thérien-Aubin, A. Klinkova, E. M. Larin, A. Querejeta-Fernández, L. Han, H. L. Xin, O. Gang, E. B. Zhulina, M. Rubinstein, E. Kumacheva, Surface patterning of nanoparticles with polymer patches. *Nature* **538**, 79–83 (2016).
35. K. Gao, L. T. Kearney, J. A. Howarter, Planar phase separation of weak polyelectrolyte brushes in poor solvent. *J. Polym. Sci. B.* **55**, 370–377 (2017).
36. V. Koutsos, E. W. van der Vegte, E. Pelletier, A. Stamouli, G. Hadziioannou, Structure of chemically end-grafted polymer chains studied by scanning force microscopy in bad-solvent conditions. *Macromolecules* **30**, 4719–4726 (1997).
37. M. Tebbe, E. Galati, G. C. Walker, E. Kumacheva, Homopolymer nanolithography. *Small* **13**, 1702043 (2017).
38. D. Murakami, Y. Norizoe, Y. Higaki, A. Takahara, H. Jinnai, Direct characterization of in-plane phase separation in polystyrene brush/cyclohexane system. *Macromolecules* **49**, 4862–4866 (2016).
39. G. Hadziioannou, S. Patel, S. Granick, M. Tirrell, Forces between surfaces of block copolymers adsorbed on mica. *J. Am. Chem. Soc.* **108**, 2869–2876 (1986).
40. J. N. Israelachvili, *Intermolecular and Surface Forces* (Elsevier, ed. 3, 2011), chap. 13.
41. O. Azzaroni, S. Moya, T. Farhan, A. A. Brown, W. T. S. Huck, Switching the properties of polyelectrolyte brushes via "hydrophobic collapse". *Macromolecules* **38**, 10192–10199 (2005).
42. T. Farhan, O. Azzaroni, W. T. S. Huck, AFM study of cationically charged polymer brushes: Switching between soft and hard matter. *Soft Matter* **1**, 66–68 (2005).
43. B. Zappone, M. Ruths, G. W. Greene, G. D. Jay, J. N. Israelachvili, Adsorption, lubrication, and wear of lubricin on model surfaces: Polymer brush-like behavior of a glycoprotein. *Biophys. J.* **92**, 1693–1708 (2007).
44. E. B. Zhulina, M. Rubinstein, Lubrication by polyelectrolyte brushes. *Macromolecules* **47**, 5825–5838 (2014).
45. M. Husseman, E. E. Malmström, M. McNamara, M. Mate, D. Mecerreyes, D. G. Benoit, J. L. Hedrick, P. Mansky, E. Huang, T. P. Russell, C. J. Hawker, Controlled synthesis of polymer brushes by "living" free radical polymerization techniques. *Macromolecules* **32**, 1424–1431 (1999).
46. C. Devaux, J. P. Chapel, E. Beyou, P. Chaumont, Controlled structure and density of "living" polystyrene brushes on flat silica surfaces. *Eur. Phys. J. E. Soft Matter* **7**, 345–352 (2002).
47. T. Hoshino, Y. Tanaka, H. Jinnai, A. Takahara, Surface and interface analyses of polymer brushes by synchrotron radiation. *J. Phys. Soc. Jpn.* **82**, 021014 (2013).
48. J. Israelachvili, Y. Min, M. Akbulut, A. Alig, G. Carver, W. Greene, K. Kristiansen, E. Meyer, N. Pesika, K. Rosenberg, H. Zeng, Recent advances in the surface forces apparatus (SFA) technique. *Rep. Prog. Phys.* **73**, 036601 (2010).
49. M. J. Stevens, K. Kremer, The nature of flexible linear polyelectrolytes in salt free solution: A molecular dynamics study. *J. Chem. Phys.* **103**, 1669–1690 (1995).

Funding: J.Y., B.K.B., and M.T. thank the U.S. Department of Energy Office of Science, Program in Basic Energy Sciences, Materials Sciences and Engineering Division. This material is based upon work supported by the National Science Foundation under grants no. NSF CMMI (Division of Civil, Mechanical, and Manufacturing Innovation)–1562878 (X.X.) and NSF CMMI-1161475 (M.R.). N.E.J. thanks the Argonne National Laboratory Maria Goeppert Mayer Named Fellowship for support. We acknowledge the computing resources provided on Blues, a high-performance computing cluster operated by the Laboratory Computing Resource Center at Argonne National Laboratory. **Author contributions:** N.E.J. performed the MD simulations and data analysis. J.Y. synthesized the PSS brushes and performed the SFA experiments and data analysis. X.X. and M.R. performed the AFM experiments and data analysis. J.Y., B.K.B., M.T., and J.J.d.P. designed the research. J.Y., X.X., N.E.J., B.K.B., M.R., M.T., and J.J.d.P. wrote the manuscript. **Competing interests:** The authors declare that they have no competing interests. **Data and materials availability:** All data needed to evaluate the conclusions in the paper are present in the paper and/or the Supplementary Materials. Additional data related to this paper may be requested from the authors.

Submitted 19 June 2017
Accepted 6 November 2017
Published 8 December 2017
10.1126/sciadv.aao1497

Citation: J. Yu, N. E. Jackson, X. Xu, B. K. Brettmann, M. Ruths, J. J. de Pablo, M. Tirrell, Multivalent ions induce lateral structural inhomogeneities in polyelectrolyte brushes. *Sci. Adv.* **3**, eaao1497 (2017).